Energy Conversion and Management 334 (2025) 119834

Contents lists available at ScienceDirect

Energy Conversion and Management

journal homepage: www.elsevier.com/locate/enconman

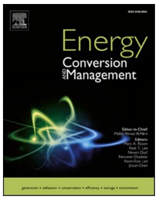

Research Paper

Design and optimization of printed thermoelectric generators for integration into plate heat exchangers in district heating applications

Muhammad Irfan Khan [a], Leonard Franke [a], Andres Georg Rösch [a], Md. Mofasser Mallick [a], Uli Lemmer [a,b,c,*]

[a] Light Technology Institute, Karlsruhe Institute of Technology (KIT), Engesserstrasse 13, 76131 Karlsruhe, Germany
[b] InnovationLab GmbH, Speyerer Strasse 4, 69115 Heidelberg, Germany
[c] Institute of Microstructure Technology, Karlsruhe Institute of Technology (KIT), Hermann-von-Helmholtz-Platz 1, 76344 Eggenstein-Leopoldshafen, Germany

ARTICLE INFO

Keywords:
Thermoelectrics
Printed TEGs
Plate heat exchangers
District heating

ABSTRACT

Printed thermoelectric generators (TEGs) can be a promising solution for waste heat recovery. Due to large variations in heat source and heat sink geometries, heat transfer coefficients, and temperatures found for the different applications, a versatile manufacturing approach is needed for TEGs in this field. Shape-conformable TEGs can be manufactured using printing technologies offering a low-cost and scalable manufacturing method. This paper presents design optimization for printed TEGs that can be integrated with a water-to-water corrugated plate heat exchanger (PHE) to realize a micro-CHP system in district heating applications. We explicitly state the mass flow rates, temperatures, and heat flux boundary conditions for the PHE. Based on these conditions, we optimize the TEGs using a Python-implemented model in conjunction with COMSOL simulations. The fill factor is a degree of freedom in TEG design that allows to balance material consumption, mechanical properties, and power density. By compromising on a portion of low-grade heat transfer, the proposed micro-CHP (hybrid PHE-TEG) system produces high-grade electrical power densities of 355 W/m^2 and 710 W/m^2 for TEG fill factors of $F = 0.5$ and $F = 1.0$, respectively. However, the optimal TEG leg thickness for $F = 0.5$ is lower (190 μm) than for $F = 1.0$ (210 μm), and the former case exhibits more compromise on PHE performance than latter one. Lastly, the total system cost (in €), cost per watt (in €/W), and levelized cost of electricity (LCOE, in €-ct/kWh) are analyzed and reported for two system sizes—one with a 0.5 m^2 area and the other with a 1 m^2 area. A system size with 0.5 m^2 area showed higher cost of electricity of 11.2 €/W and 10 €-ct/kWh for $F = 0.5$, while for $F = 1.0$ they were 6.2 €/W and 6 €-ct/kWh. In comparison to 0.5 m^2, 1 m^2 system size showed lower cost of electricity of 8.1 €/W and 7 €-ct/kWh for $F = 0.5$, while for $F = 1.0$ cost values were 4.7 €/W and 4 €-ct/kWh.

1. Introduction

A substantial proportion of the global primary energy production is lost to the environment as waste heat through exhaust systems. Among the different available grades of thermal energy, low-grade energy (<230 °C) [1] is a ubiquitous byproduct of several industrial and power generation processes. Nevertheless, compared to medium and high grades, it is also the most challenging to recover thermodynamically because of its relatively small exergy [2]. Low-grade waste heat originates from various sources, including the human body, which maintains a temperature of 37 °C. In a typical daily routine, the body releases thermal energy to the environment with a heat loss rate of 100 W [3]. Likewise, oceans are an immense reservoir of thermal energy collected from the sun and could generate 20 times the total electricity demands of the United States if just 0.1 % of this thermal energy is transformed into electricity [4]. Other sources include numerous material process industries [5–7], low-temperature geothermal heat sources [8], refrigeration and air conditioning [9], solar thermal systems as well as photovoltaics [10]. The takeaway is that there are a lot of low-grade thermal energy sources. Still, there has not been significant technological advancement in the cost-effective way of transforming or recovering this energy [11].

Thermoelectric (TE) technology seems to be a feasible and promising solution for converting this low-grade thermal energy into usable electrical energy. It has many merits over other approaches, including

---

* Corresponding author at: Light Technology Institute, Karlsruhe Institute of Technology (KIT), Engesserstrasse 13, 76131 Karlsruhe, Germany.
E-mail address: uli.lemmer@kit.edu (U. Lemmer).

https://doi.org/10.1016/j.enconman.2025.119834
Received 26 January 2025; Received in revised form 27 March 2025; Accepted 20 April 2025

Nomenclature

Symbols

W	PHE plate width, (m)
Y	distance b/w centers of plate's ports, (m)
L	active length, (m)
b	mean channel spacing, (m)
t	thickness, (m)
U	overall HTC, (W/m^2. K)
T	temperature, (K)
Ψ	thermal resistance, (K/W)
$\dot{q}$	heat flow, (W)
h	convection HTC, (W/m^2. K)
A	area, (m^2)
Nu	Nusselt number
Re	Reynolds number
Pr	Prandtl number
D	hydraulic diameter, (m)
c_p	specific heat capacity, (J/kg. K)
G	mass flux, (kg/m^2)
$\dot{m}$	fluid mass flow rate, (kg/s)
N_t	no. of PHE plates
N_{pass}	no. of passages/channel
C	capacity rate (W/K)
F	fill factor
Z	figure of merit (1/K)
r	area ratio
n_t	no. of thermocouples
P	power density, (W/m^2)
R	electrical resistance, (Ω)
I	current, (A)
V	voltage, (V)
K	TEG thermal conductance, (W/K)
I_0	capital investment, (€)
d	discount rate
E	generated electrical energy (kWh)

Greek Symbols

λ	corrugation pitch, (m)
f	friction factor
β	chevron angle, (°)
φ	surface enlargement factor
κ	thermal conductivity, (W/m. K)
μ	dynamic viscosity, (kg·m·s)
α	seebeck coefficient, (V/K)
σ	electrical conductivity, (S/m)
Δ	difference

Subscripts and superscripts

pl	plate
s	heat source
a	heat sink
h	hot side
c	cold side
in	inlet
out	outlet
int	internal
oc	open circuit
cont	contacts
load	load (external)
simple	PHE without TEGs
hybrid	PHE with TEGs
conv	convection heat transfer
cond	conduction heat transfer
f	fluid
w	near wall
cs	cross section
eff	effective
tot	total
max	maximum
n	n-type
p	p-type
filler	filler material
m	lifetime
y	respective year

Abbreviations

TEGs	thermoelectric generators
PHE	plate heat exchanger
CHP	combined heat and power
TES	thermal energy storage
5GDH	5th generation district heating
HP	heat pump
HTC	heat transfer coefficient
CFD	computational fluid dynamics
PTC	parametric technology corporation
LCOE	levelized cost of electricity

robustness, cost-effectiveness, absence of noise, reliability, and scalability [12,13]. A thermoelectric generator (TEG) uses the Seebeck effect to convert thermal energy directly into electrical energy. It is long-lasting and has no moving parts, enabling a vibration and friction-free operation [14]. TEGs can also be manufactured in a plethora of shapes and sizes. These devices comprise several thermocouples (n-type and p-type) connected electrically in series and thermally in parallel. A simple configuration of a planar TEG is shown in Fig. 1. The device is kept between two thermal reservoirs to utilize the temperature difference for electrical power generation.

District heating systems can be regarded as CHP systems, which are viable for waste heat recovery since they simultaneously provide heat at useful temperatures and electrical power [2,15]. Utilizing the TEGs to develop a micro-CHP system could be a potential solution to improve energy efficiency. TEGs might also improve the living conditions in suburban and off-grid locations, especially in times of emergency [16]. Also, residential and industrial buildings have several heating demands at specific temperatures. Many residential and commercial buildings, especially in Europe, have already been built with a connection to hot water supply networks from the district heating systems or large industries [2]. Thus, the interest in micro-CHP systems develops for a variety of reasons. First, micro-CHP systems improve overall fuel efficiency by better using the hot water's exergy. Second, these systems could be an option to augment the variability and uncertainty of most renewable energy systems, such as solar and wind [17], and improve energy security in places prone to power shortages. Third, the environmental merits of these systems, such as reducing CO_2 emissions for a specific output, contribute to their appeal [18]. Currently, the paradigm of high temperature district heating (typically reaching or exceeding 100 °C) is shifting to 5th generation district heating (5GDH) system, also called cold or energy-efficient district heating (see Fig. 2) [19–21]. Several pilot projects have already been installed and are actively operating in Europe. The 5GDH system is an innovative concept for thermal energy distribution, characterized by low operating temperatures ($<$ 30 °C). Unlike 2nd generation ($>$ 100 °C), 3rd generation ($<$ 100 °C), and 4th generation ($<$ 70 °C) networks, which suffer from

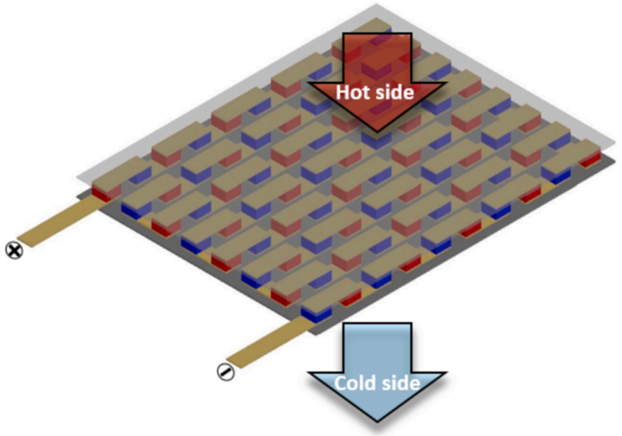

Fig. 1. A planar TEG module between two thermal reservoirs.

higher thermal losses, 5GDH significantly minimizes these losses in distribution [22]. Additionally, 5GDH can improve the system performance by utilizing several available low-grade heat sources including renewables (solar thermal, geothermal, biomass), industrial waste heat, thermal energy storage, and low-temperature CHP. However, more conventional high temperature traditional district heating systems are unable to exploit these low-grade thermal energy sources. Since there are many available low-grade heat sources (∼ 70–80 °C) on one side and continuous cold-water loop (∼ 5–20 °C) of 5GDH on the other, these two reservoirs become a point of interest to deploy cost-effective TEGs and asses their potential. Also, heat dissipation from the cold side of TEGs has always been a critical and challenging aspect [23]. However, in this case, the cold-water loop of the 5GDH system can serve as an efficient heat sink, effectively addressing this issue.

While there have been numerous research efforts on TEGs-integrated CHP systems using conventional TEGs [16,24–27], the focus of this work is on mechanically flexible and *fully printed* TEGs that can be geometrically customized for the complex surfaces of the heat exchanger. Besides geometrical customization printed TEGs offer potentially low manufacturing costs for large and scalable mass production [28].

In this work, we optimally design printed TEGs to be integrated with a water-to-water plate heat exchanger (Sigma M 7 NBL from APi Group), aiming to propose a micro-CHP system in district heating applications, along with a detailed cost analysis. This water-to-water PHE application scenario is chosen for TEG integration due to its efficient heat transfer, which is crucial for optimizing TEG performance. Additionally, its smooth sinusoidal plate profile is a comparatively good fit for integrating printed TEGs. Here, we also compare the performance of PHE without TEGs (simple PHE) and PHE integrated with TEGs (hybrid PHE-TEG system). The paper is divided into four sections: Introduction, Modeling, Results and Discussion, and Conclusion.

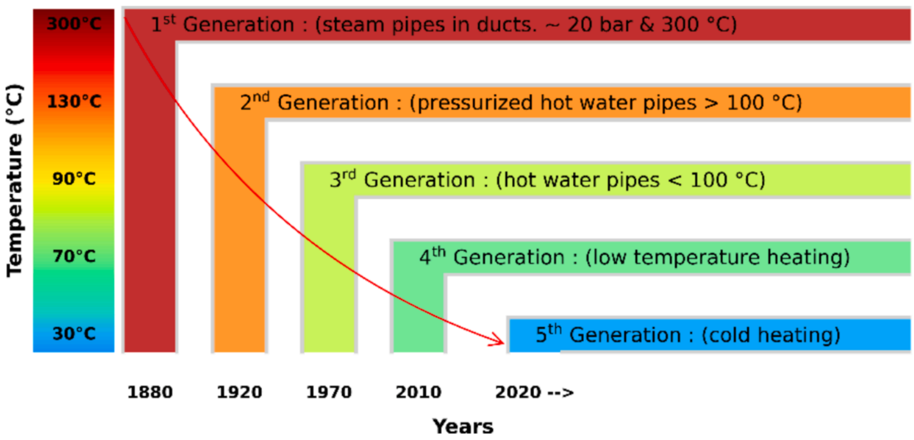

Fig. 2. Development of district heating (DH) systems.

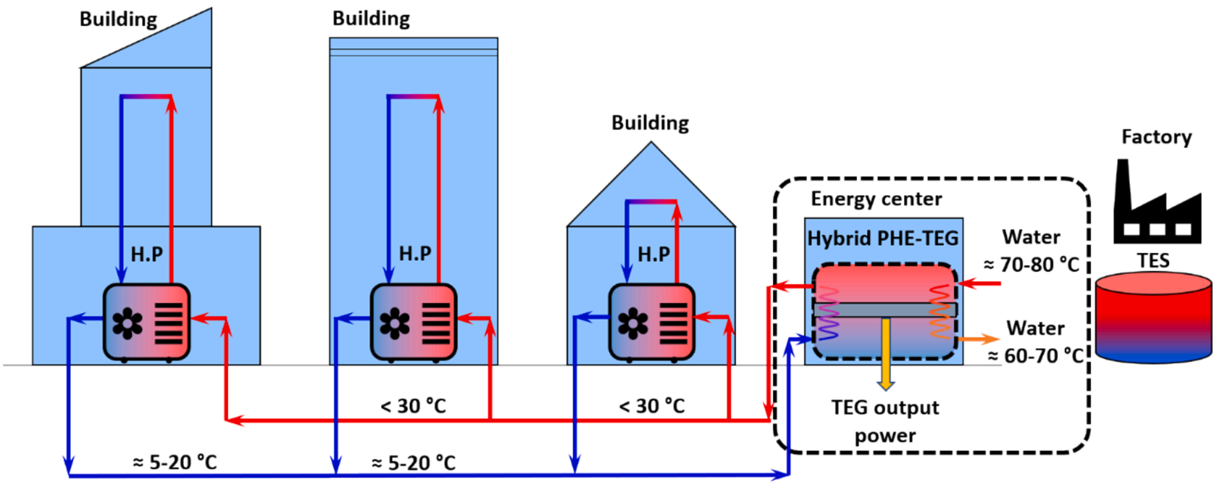

Fig. 3. Conceptual micro-CHP system with the hybrid PHE-TEG system in 5GDH.

Table 1
Characteristics of PHE by the manufacturer.

No. of sections	1	2
Fluid	Cold water	Hot water
Capacity	1959 l/h	2000 l/h
Plate grouping	4 channels	5 channels
Pressure drop	0.17 bar	0.1 bar
No. of plates	10 (can be expanded to 35 plates)	
Heat exchange surface	0.5 m^2 (area of 8 active plates)	

Table 2
Geometrical parameters of PHE chevron plate used in the model.

Geometrical parameters	Value
Plate width, W (mm)	128
Vertical distance between centers of ports, Y (mm)	480
Active plate length, L_{pl} (mm)	410
Mean channel spacing, b (mm)	3.15
Plate thickness, t_{pl} (mm)	0.6
Corrugation pitch, λ (mm)	11.13
Chevron angle, β (°)	61.7
Surface enlargement factor,φ	1.172
Plate thermal conductivity, κ_{pl} (W/m. K)	15

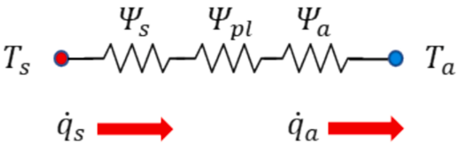

Fig. 4. Thermal circuit of a simple PHE.

2. Modeling

2.1. Micro-CHP system

The proposed micro-CHP system comprises a PHE Sigma M 7 NBL from APi Group with the TEGs integrated on its corrugated plates. This system was inspired by Kazuaki Yazawa's research on waste heat recovery using the CHP-TEG heat exchanger concept [2]. In this research, hot water, with a temperature around 80 °C is supplied to this system either from a factory, a thermal energy storage (TES) unit, a geothermal energy source, or another source. In the cold side loop, cold water at around 20 °C enters and absorbs heat from the hot side, raising its temperature to approximately 25 to 30 °C. This low-temperature heated water, now at 25 to 30 °C, can be efficiently utilized for district heating within the 5th generation district heating concept (shown in Fig. 3). Localized heat pumps (H.P) then extract thermal energy from low-temperature water to meet specific heating requirements [22,29]. The output power from the TEGs may likely be used locally. Note that pumps could consume some of the electrical power output. Consequently, a trade-off arises between the pumping power required and the net power output from the TEGs. The ideal micro-CHP system is shown in Fig. 3. This system could also be a bottoming cycle approach for harvesting exhaust heat that would otherwise be wasted.

2.1.1. Plate heat exchanger (PHE)

The hybrid PHE-TEG is a main component of the above micro-CHP system. Tables 1 and 2 show the properties of the PHE used in this component and its plate's geometrical parameters, respectively.

The overall heat transfer coefficient (HTC) is an important parameter that measures a heat exchanger's overall thermal conductance. It represents the sum of all the individual thermal resistances to heat transfer over the heat exchanger surface. For a simple PHE, U_{simple} is calculated from Eq. (2) (if convection and conduction areas are different) and Eq. (3) (if convection and conduction areas are equal). For better understanding, a thermal circuit for a simple PHE has also been drawn in Fig. 4.

$$U_{simple} = \frac{1}{\Psi_s + \Psi_{pl} + \Psi_a} \tag{1}$$

$$U_{simple}\cdot A = \frac{1}{\left(\frac{1}{h_s\cdot A_1}\right)_{conv} + \left(\frac{t_{pl}}{\kappa_{pl}\cdot A_2}\right)_{cond} + \left(\frac{1}{h_a\cdot A_3}\right)_{conv}} \tag{2}$$

$$U_{simple} = \frac{1}{\left(\frac{1}{h_s}\right)_{conv} + \left(\frac{t_{pl}}{\kappa_{pl}}\right)_{cond} + \left(\frac{1}{h_a}\right)_{conv}} \tag{3}$$

In the above equation, the convection heat transfer coefficients of the hot and cold fluids h_s and h_a are needed to calculate U_{simple}. The Nusselt number Nu relation:

$$h = \frac{Nu\cdot k_f}{D} \tag{4}$$

is used to compute the convection heat transfer coefficients for both hot and cold fluids. Here, k_f and D are the flowing fluid's thermal conductivity and the chevron-type plate's hydraulic diameter, respectively.

$$D = \frac{2b}{\varphi} \tag{5}$$

In Eq. (5) b and φ are the mean channel spacing and surface area enlargement factor for the chevron-plate, respectively. For sinusoidal corrugations, φ is calculated by the following an approximating formula (with an error < 2 %) [30]:

$$\varphi(X) \approx \frac{1}{6}\left(1 + \sqrt{1+X^2} + 4\sqrt{1+X^2/2}\right) \tag{6}$$

where $X = \pi b/\lambda$ and λ is the pitch or wavelength of the sinusoidal corrugation, as shown in Fig. 9.

The Nusselt number Nu is calculated from the Martin Correlation for chevron-type plate heat exchangers (Eq. (7) [30].

$$Nu = 0.205Pr^{0.333}\cdot\left(\frac{\mu_f}{\mu_w}\right)^{\frac{1}{6}}\cdot\left(f\cdot Re^2\cdot sin(2\beta)\right)^{0.374} \tag{7}$$

$$\frac{1}{\sqrt{f}} = \frac{\cos(\beta)}{\sqrt{0.045\tan(\beta) + 0.09\sin(\beta) + \frac{f_o}{\cos(\beta)}}} + \frac{1-\cos(\beta)}{\sqrt{3.8f_1}} \tag{8}$$

$$f_o = \frac{16}{Re}\ \&\ f_1 = \frac{149.25}{Re} + 0.9625\ when\ Re < 2000 \tag{9}$$

$$f_o = (1.56\ln(Re) - 3)^{-2}\ \&\ f_1 = 9.75Re^{-0.289}\ when\ Re > 2000 \tag{10}$$

Here, f is the friction factor developed by Martin [30] in terms of β, the chevron angle of the PHE plate as shown in Fig. 9. The friction factor is different in laminar and turbulent flow regimes (see Eq. (9) and Eq. (10) [31,32]. Furthermore, μ_f and μ_w are dynamic viscosities for bulk fluid and fluid near the wall surface, respectively. Now the unknown terms in Eq. (7) are the Reynolds no. Re and the Prandtl no. Pr which are calculated by the following relations:

$$Pr = \frac{\mu_f\cdot c_p}{k_f} \tag{11}$$

$$Re = \frac{G_f\cdot D}{\mu_f} \tag{12}$$

Where, c_p is the specific heat of fluid and G_f is the mass flux and is calculated by the following formula:

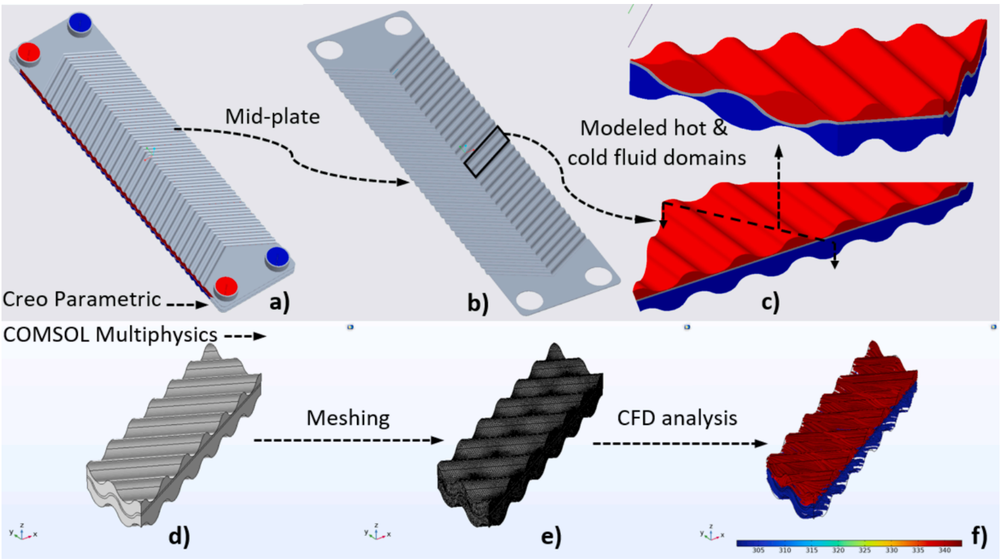

Fig. 5. Modeling and simulation of simple PHE (for validation).

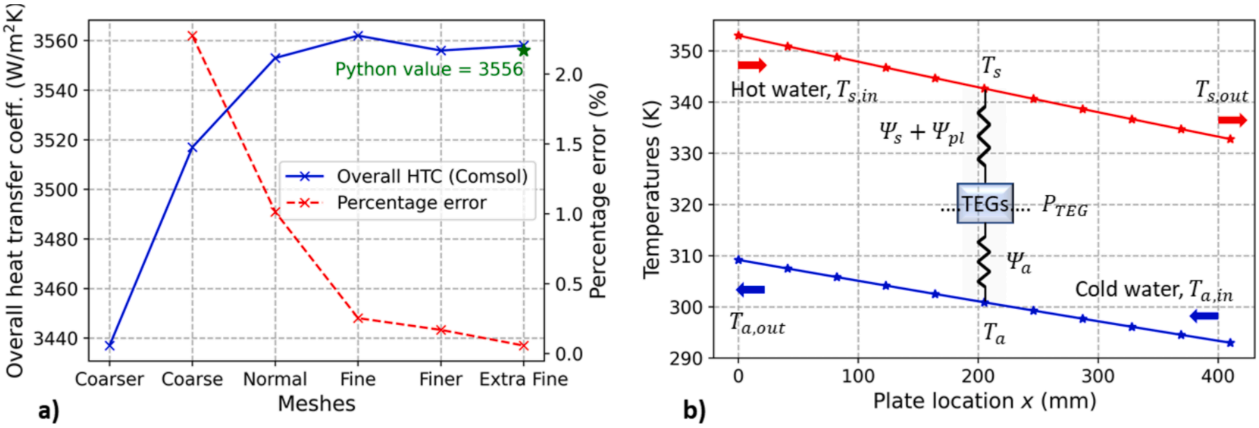

Fig. 6. a) Mesh independence study and b) temperature profiles vs plate location (simple PHE).

$$G_f = \frac{\dot{m}_f}{A_{cs}} \tag{13}$$

$$A_{cs} = b \cdot W \cdot \left(\frac{N_t - 1}{2 \cdot N_{pass}}\right) \tag{14}$$

Here, $\dot{m}_f$ is the mass flow rate of fluid and A_{cs} is the cross-sectional area through which fluid passes. N_t is the total number of PHE plates and N_{pass} is the number of passages per channel (1 in this case). Combining these equations, we can analytically calculate convection heat transfer coefficients for both fluids [30]. Thus, we can get the overall heat transfer coefficient U_{simple} for a PHE from Eq. (3) which results in 3556 W/m^2. K.

2.1.2. Python model validation

To ensure the reliability and accuracy of the Python-implemented model, the predicted overall heat transfer coefficient was compared with the one from CFD simulations conducted using COMSOL Multiphysics 6.2. Firstly, a 3D section of a corrugated plate heat exchanger, comprising both hot and cold fluid domains, was modeled in PTC Creo Parametric 10.0. The model was then imported into COMSOL, where materials were assigned to each domain (refer to Fig. 5). Subsequently, mass flow and temperature boundary conditions were applied in a counterflow configuration of the heat exchanger, with hot water entering from the top and cold water from the bottom. This study employed a robust k-ε turbulence model for turbulent flow, which is commonly used in industrial applications, for CFD simulations. The entered flow was treated as a fully developed flow for both hot and cold sides.

Finally, a mesh independence study was conducted, starting with a coarser mesh and progressing to an extra-fine mesh. The overall heat transfer coefficient and the corresponding percentage errors were evaluated at each stage, as shown in Fig. 6a). After fine mesh and refining the mesh further, the values began to oscillate with a very low percentage error (< 0.1 %), indicating that the solution was no longer significantly affected by mesh refinement. COMSOL simulation predicted the overall heat transfer coefficient of 3558 W/m^2. K at the extra-fine mesh, which shows strong agreement with the value predicted by the Python model.

When hot and cold fluids flow along the plate length in a PHE, the temperatures of the fluids vary at each location x, and are determined by the equations Eq. (15) and (16) for the counter flow case [33]:

$$T_s(x) = \left(e^{-\left(1+\frac{C_s}{-C_a}\right)\cdot\left(\frac{U_{simple}\cdot A_{tot}}{C_s}\cdot\frac{x}{L_{pl}}\right)} \cdot \left(T_{s,in} - T_\infty\right) \right) + T_\infty \tag{15}$$

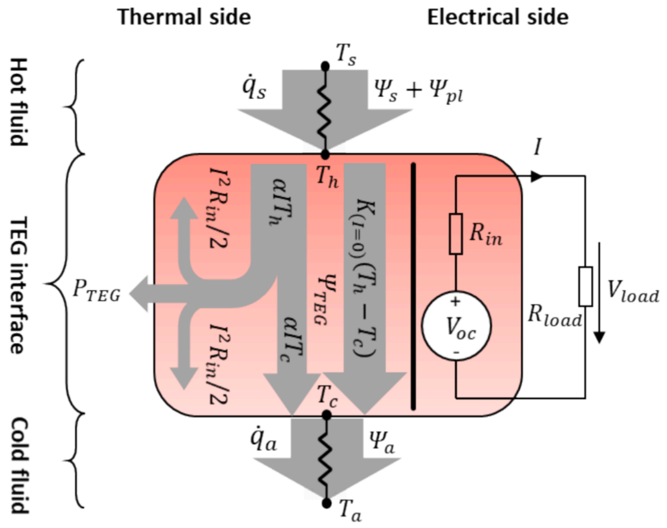

Fig. 7. Schematic thermoelectrical picture of the TEG.

$$T_a(x) = \left(e^{-\left(1+\frac{-C_a}{C_s}\right)\cdot\left(\frac{U_{simple}\cdot A_{tot}}{-C_a}\cdot\frac{x-L_{pl}}{L_{pl}}\right)}\cdot(T_{a,in} - T_\infty)\right) + T_\infty \tag{16}$$

Where, $C = \dot{m}_f \cdot c_p$ is the heat capacity rate, defined as product of mass flow rate and specific heat capacity of the fluids. T_∞ is calculated by the following relation:

$$T_\infty = \frac{\frac{C_s}{-C_a}\cdot T_{s,in} + T_{a,in}e^{\left(1+\frac{C_s}{-C_a}\right)\cdot\left(\frac{U_{simple}\cdot A_{tot}}{C_s}\right)}}{\frac{C_s}{-C_a} + e^{\left(1+\frac{C_s}{-C_a}\right)\cdot\left(\frac{U_{simple}\cdot A_{tot}}{C_s}\right)}} \tag{17}$$

In the above equations Eq. (15) to Eq. (17), A_{tot} is the active area of the heat transfer in all 9 channels (8 active plates) shown in Fig. 9 and it is calculated by:

$$A_{tot} = A_{eff}\cdot(N_t - 2) \tag{18}$$

$$A_{eff} = \varphi\cdot L_{pl}\cdot W \tag{19}$$

Where, A_{eff} is the effective area of one plate.

The anticipated temperature profiles for both fluids along the flow direction are presented in Fig. 6b).

2.1.3. *Plate heat exchanger integrated with TEGs (hybrid PHE-TEG)*

In this work, we consider a planar thermoelectric device, with the selection of the optimal thickness and fill factor of the TEGs thoroughly discussed in our previous work [28]. Fill factor and leg thickness are two important geometrical parameters for designing a TEG device, ensuring simultaneous thermal and electrical impedance matching. This optimum condition is met only when TEG's thermal resistance (Ψ_{TEG}) and electrical resistance (R_{int}) match with the thermal contact resistances ($\Psi_{cont} = (\Psi_s + \Psi_{pl}) + \Psi_a$) and load electrical resistance (R_{load}) respectively (see Fig. 7). At each fill factor, there is unique leg thickness value to achieve this condition. Here, we choose two fill factors F = 0.5 and F = 1.0, and calculate corresponding leg thicknesses where this condition is met.

To get the maximum effective device figure of merit Z_{max}, a generalized geometry condition was developed for equal thicknesses of n-type, p-type, and filler material ($t_n = t_p = t_{filler} = t$).

$$Z_{max} = \frac{\left(\alpha_p - \alpha_n\right)^2}{\left(\sqrt{\frac{\kappa_n}{\sigma_n} + \frac{\kappa_{filler}}{\sigma_n}\cdot\frac{1-F}{F}} + \sqrt{\frac{\kappa_p}{\sigma_p} + \frac{\kappa_{filler}}{\sigma_p}\cdot\frac{1-F}{F}}\right)^2} \tag{20}$$

Where, $\alpha_p, \alpha_n, \sigma_p, \sigma_n, \kappa_p, \kappa_n$ are the Seebeck coefficients, electrical conductivities and thermal conductivities of the n-type and p-type TE materials respectively and κ_{filler} is the thermal conductivity of filler material. Additionally, Eq. (22) provides general expressions for the optimal cross-sectional areas A_n and A_p:

$$r = \frac{A_n}{A_p} = \sqrt{\frac{\frac{\kappa_p}{\sigma_n} + \frac{\kappa_{filler}}{\sigma_n}\cdot\frac{1-F}{F}}{\frac{\kappa_n}{\sigma_p} + \frac{\kappa_{filler}}{\sigma_p}\cdot\frac{1-F}{F}}} \tag{21}$$

$$A_n = \frac{F\cdot A_{TEG}}{n_t\cdot\left(\frac{1}{r}+1\right)}\ ,\ A_p = \frac{F\cdot A_{TEG}}{n_t\cdot(r+1)} \tag{22}$$

Material properties of the printed TEG used in this study are reported in our previous work [34]. Besides this active material, the TEG device is supposed to be filled with filler material (such as polystyrene) with a low thermal conductivity of 0.1 W/m. K.

The flexible printed TEGs are designed to integrate directly onto the corrugated plates of the PHE. To illustrate the simulation model, a section of the hybrid PHE-TEG system for the aforementioned micro-CHP system is shown in Fig. 8, considering two cases: case-I with F = 0.5 and case-II with F = 1.0. For each case, two thermocouples were simulated in COMSOL under convective heat transfer boundary conditions, with TEGs applied first into the cold channel and then into the hot channel, and the results were compared. Note, convection heat transfer coefficients h_a and h_s for hybrid PHE-TEG system were calculated using the Python-based model (Eq. (4) to Eq. (14) as before, since the heat exchanger plate profiles (b and φ) remains unchanged after installing the TEGs (see Fig. 9). The proposed TEG layout for this hybrid PHE-TEG

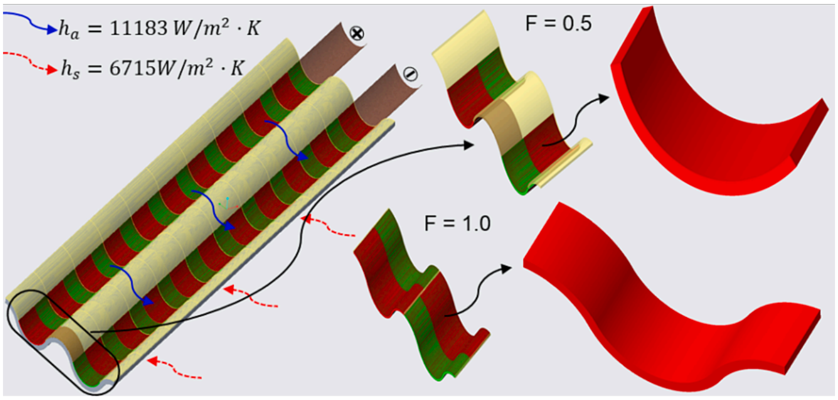

Fig. 8. A portion of hybrid PHE-TEG for simulation (case-I F = 0.5, case-II F = 1.0).

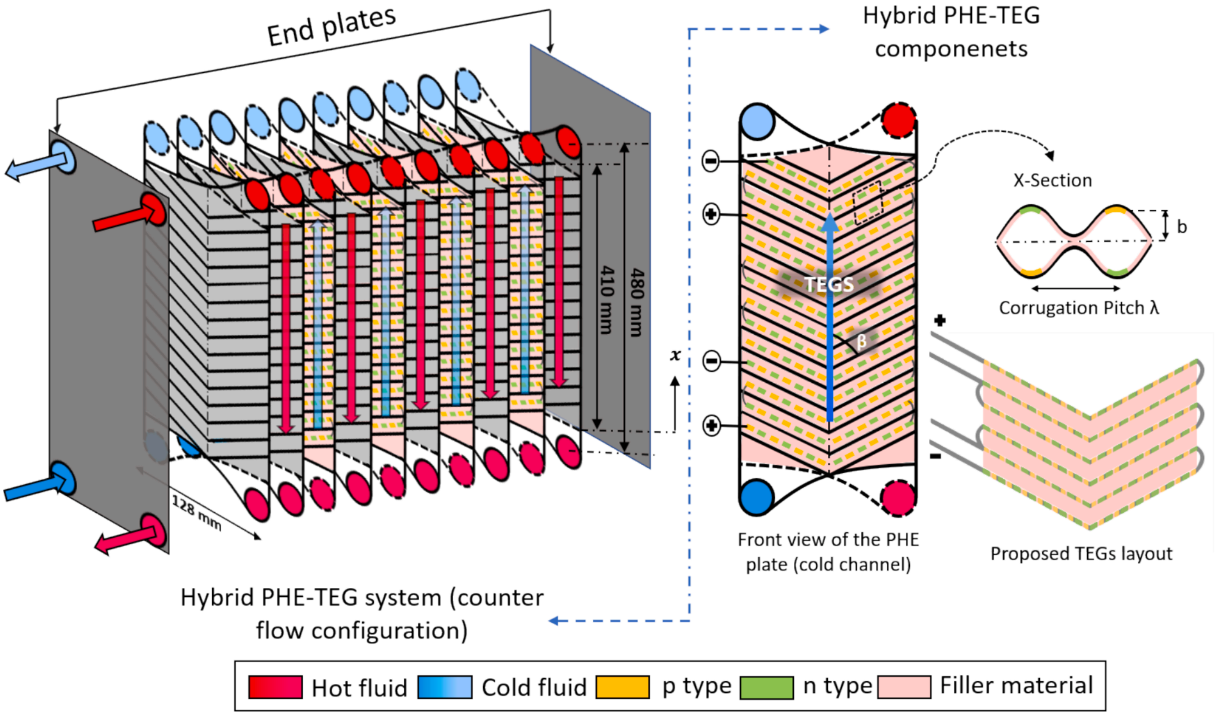

Fig. 9. Components of hybrid PHE-TEG system (TEGs in the cold channel).

system is also shown in Fig. 9.

Additionally, the following assumptions were made for our heat transfer and TEG power output analysis:

- The plate heat exchanger is adiabatic to the surrounding environment.
- Fluid properties are considered at the mean temperatures of the respective channel fluid.
- The heat flux from hot to cold fluid will completely pass through the TEGs, i.e., there is no heat loss from a thermal shunt.
- Only intrinsic TEG resistance is considered; electrical contact resistances are neglected.
- No thermal contact resistance between the PHE plate and the TEGs was considered.

2.1.4. Cost analysis

This novel hybrid PHE-TEG system provides a dual functionality of heat transfer and power production. In this study, we also analyzed the economic and performance metrics of the system including:

Total system cost: The overall capital cost (in €) required to construct this hybrid PHE-TEG.
Cost per watt: The cost of generating one watt of electric power (in €/W), calculated as the ratio of total system cost to the rated electric power produced.

Lastly, we computed the levelized cost of electricity (LCOE, in €-ct/kWh), a key metric that shows the cost per unit of electricity produced over the system's lifetime, in order to assess economic viability in this study. The LCOE is calculated as the ratio of the system's total lifetime cost to its total lifetime electricity generation.

$$LCOE = \frac{Capital\ cost}{Life\ time\ electricity\ output} \tag{23}$$

As TEGs will not cause any maintenance and operational costs, it can be calculated as [35]:

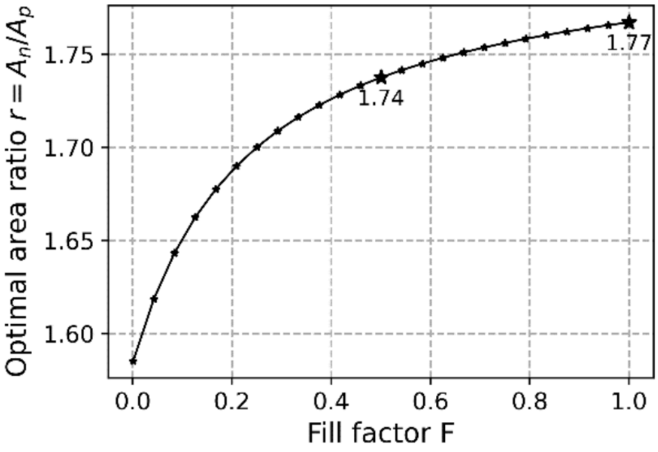

Fig. 10. Optimal area ratio r vs fill factor F.

$$LCOE = \frac{I_0}{\sum_{y=1}^{m} \frac{E_y}{(1+d)^y}} \tag{24}$$

This metric highlights the system's cost-effectiveness, here, I_0 is the total initial investment, m is the total lifetime in years, d is the discount rate, y is the respective year, and E_y is the electricity generated per year.

3. Results and Discussion

3.1. Optimal cross-sectional area calculation

A TEG device performance strongly depends upon its effective figure of merit Z. In order to maximize effective Z_{max} value for a device, reference [28] reported a generalized geometric optimization condition (refer to Eq. (21), which gives an optimal cross-sectional area ratio $r = A_n/A_p$ of n-type and p-type legs. Fig. 10 illustrates values of r at different fill factors, indicating that the cross-sectional area of the n-type leg

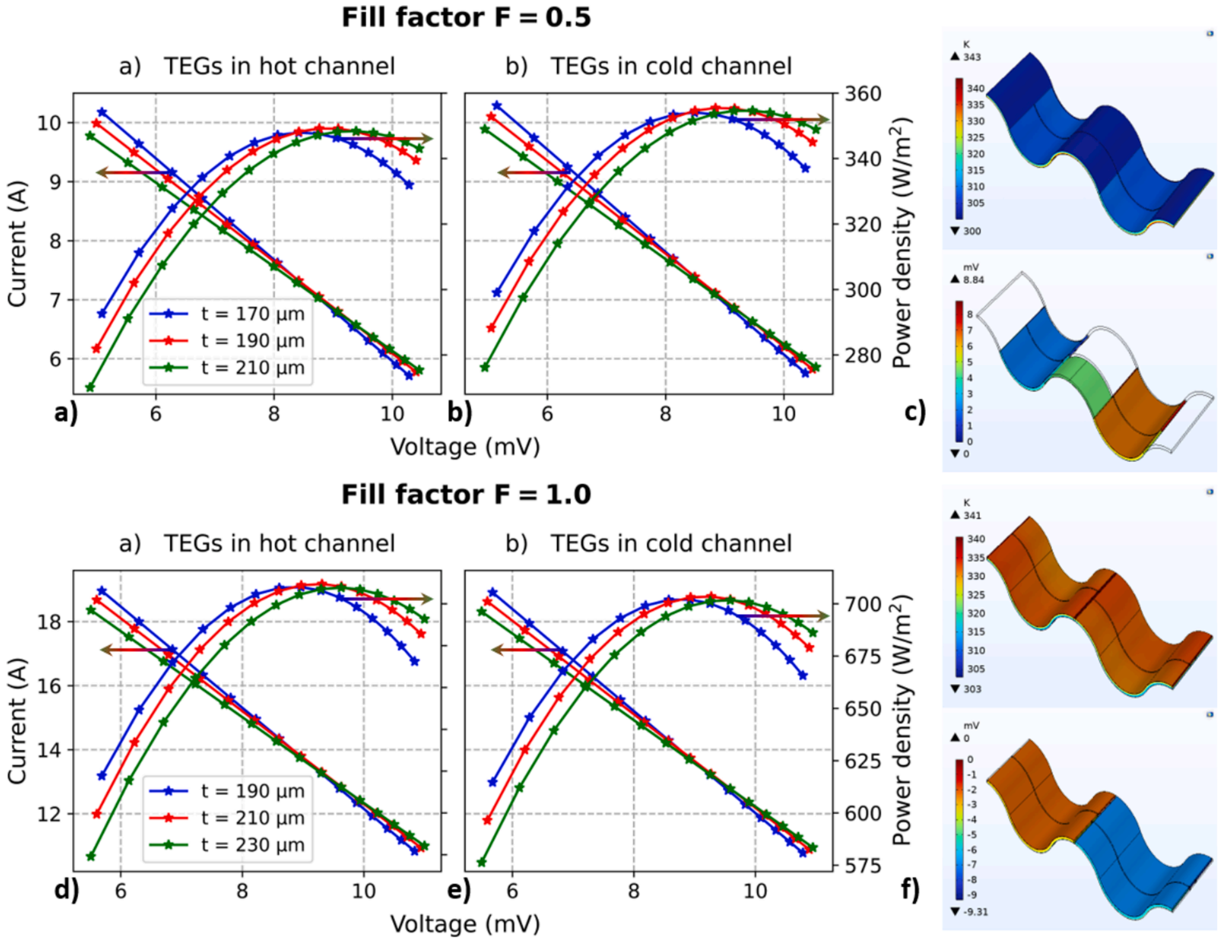

Fig. 11. Output power densities and I-V curves (case-I F = 0.5, case-II F = 1.0).

should be 1.74 times that of the p-type leg for a fill factor of F = 0.5, and 1.77 times for a fill factor of F = 1.0 for our choice of materials. This difference in area arose due to the mismatch in the thermoelectric properties of these two materials.

After determining the optimal area ratio for these two scenarios (F = 0.5 and F = 1.0), TEGs were modeled on the PHE plate, as illustrated in Fig. 8, using the calculated areas for the n-type and p-type materials for further analysis.

3.2. Optimal thickness calculation

The proper design of the TEGs for maximum power in any application environment relies on optimizing thermal and electrical resistance. Changing the thickness of the TEG at a given fill factor F is a key parameter to vary with thermal and electrical resistance and find an optimum spot. Under fixed thermal resistances of source and sink in the PHE (calculated from the analytical model described by Eqs. (1) to (14), an increase in the TEG thickness initially causes a rapid rise in the temperature difference ΔT across the TEG. On the other hand, the electrical resistance also increases linearly as the TEG thickness increases. When these two competing parameters approach a certain threshold, we notice an initial rise in power due to an increased temperature difference ΔT followed by a loss in power output due to an increase in electrical resistance with suppressed benefits in increasing thermal resistance further. This threshold refers to simultaneous matching thermal and electrical impedances to maximize power output from TEGs at given conditions. Fig. 11 presents the TEG output power densities and I-V curves at three different TEG thicknesses, plotted to determine the optimal operating conditions for the previously introduced system (hybrid PHE-TEG) in two scenarios (F = 0.5 and F = 1.0).

Fig. 11a) represents the results of a COMSOL parametric sweep study for three different TEG thicknesses, with the TEGs integrated into the hot channel. In contrast, Fig. 11b) illustrates the results when the TEGs are integrated into the cold channel. The analysis indicates that the optimal TEG thickness is 190 µm, yielding a higher power density of approximately 355 W/m^2 when integrated into the cold channel compared to the hot channel (see Fig. 11a) and 11b)). The higher power density for the cold channel is attributed to the difference in the cross-sectional areas of the thermoelectric legs exposed to the hot and cold sides. Additionally, a mismatch in convective heat transfer between the two sides contributes to this effect. The TEG generates more power when the smaller area is exposed to a relatively higher convective heat transfer coefficient, as illustrated in Fig. 8. In the second case, with a fill factor F = 1.0, the optimal TEG thickness is found to be 210 µm, resulting in a higher power density of approximately 710 W/m^2 when the TEGs are integrated into the hot channel (see Fig. 11d) and 11e)). Here, the thermoelectric leg areas are identical on both sides as shown in Fig. 8, and the power output is higher with integration into the hot channel due to the superior thermoelectric properties at higher temperatures. The 3D temperature and voltage plots from COMSOL at the maximum power point are shown in Fig. 11c) and Fig. 11f), where for F = 0.5, the TEGs are assumed to be integrated into the cold channel, and for F = 1.0, the TEGs are assumed to be integrated into the hot channel.

3.3. Transferred heat flux in the simple PHE and hybrid PHE-TEG

The heat flux transferred from the hot fluid in the simple PHE was

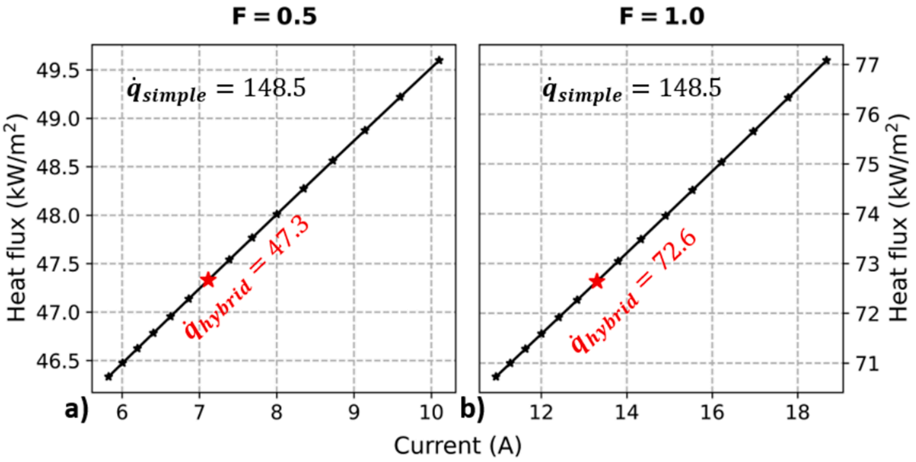

Fig. 12. Heat fluxes, simple PHE, and hybrid PHE-TEG (case-I F = 0.5, case-II F = 1.0).

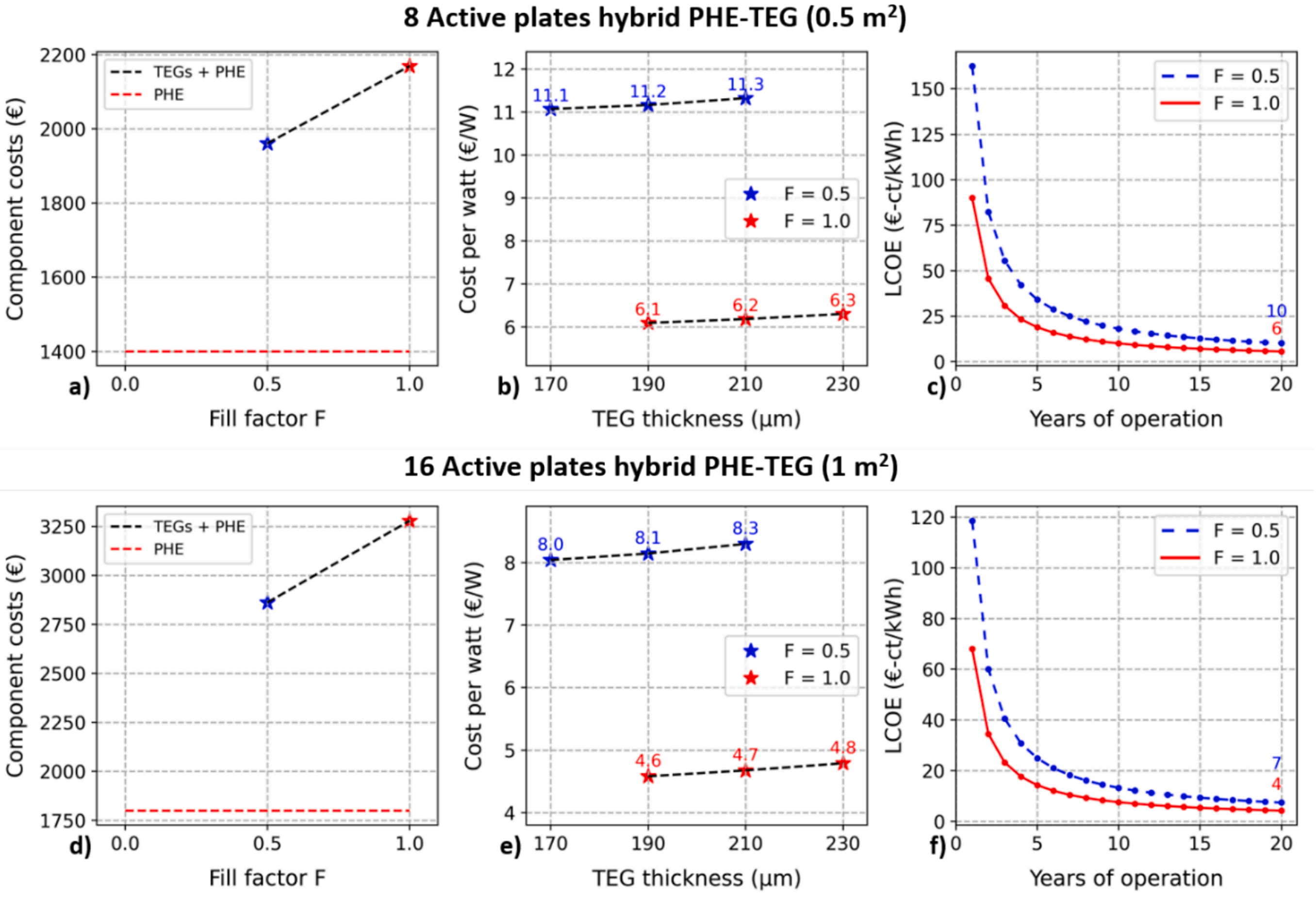

Fig. 13. System cost, cost per watt, and levelized cost of electricity (LCOE) of proposed micro CHP (hybrid PHE-TEG).

estimated to be 148.5 kW/m^2. In contrast, for the hybrid PHE-TEG system optimized for maximum TEG power generation, the transmitted heat flux is reduced to approximately 47.3 kW/m^2 and 72.6 kW/m^2 for TEG fill factors of F = 0.5 and F = 1.0, respectively (refer to Fig. 12a) and 12b)). So, this hybrid PHE-TEG introduced a compromise in transferred heat flux, as a part of some low-grade thermal energy converted into high-grade electrical energy. As a trade-off, the optimized printed TEGs are expected to generate rated electrical power densities of 355 W/m^2 and 710 W/m^2 for these two respective cases.

3.4. System cost (€), cost per watt (€/W), and levelized cost of electricity (LCOE, in €-ct/kWh)

In Fig. 13, we calculate the total system cost including heat exchanger and printed TEGs. For printed TEGs, the cost of each step, starting from the bulk material cost to ink preparation, device manufacturing, drying, sintering, and their integration into the PHE were considered. Fig. 13 illustrates the projected total component costs (in €), the cost per watt of the complete system (in €/W), and the levelized cost of electricity (LCOE, in €-ct/kWh) over a 20-year operational

Table 3
TEG fabrication cost analysis.

Components and/or steps involved	Cost	Source
p-type TE material (Bi_2Te_3)	455 €/kg	thermonamic.ecvery.com
n-type TE material (Bi_2Te_3)	425 €/kg	thermonamic.ecvery.com
Anodized aluminum substrate (Al-Al_2O_3)	125 €/kg	steinertglobal.com
Dielectric (Thermally cured insulator)	460 €/kg	https://www.dycotecmaterials.com
Contact material (Ag)	2000 €/kg	https://www.novacentrix.com
Ink preparation (Ball milling)	35.428 €/kg	Own assessment
Printing (Screen printing)	4.629 €/m^2	Own assessment
Drying (Hot plate drying)	40.26 €/kg	Own assessment
Sintering (Flash sintering)	4.03e-2 €/m^2	Own assessment

lifespan, assuming 80 % system uptime.

The first row of three subplots corresponds to the current system shown in Fig. 13, featuring a hybrid PHE-TEG with 8 active plates covering an area of 0.5 m^2. The second row of subplots represents a hybrid PHE-TEG system with double the size, comprising 16 active plates and covering an area of 1 m^2. For a fill factor F = 1.0, this doubling restores the heat transfer capacity of a PHE without TEGs. The plots demonstrate that the cost per watt and LCOE decrease as the system size increases. This is primarily because the major cost of a plate heat exchanger arises from its basic structure and mountings. The system's capacity can be expanded cost-effectively by adding more plates, which are relatively inexpensive components. Over a 20-year lifespan, the cost per kWh is estimated to be approximately 10 €-ct and 6 €-ct for fill factors F = 0.5 and F = 1.0, respectively, for the 8-plate (0.5 m^2) hybrid PHE-TEG system. For the 16-plate (1 m^2) hybrid PHE-TEG system, the cost per kWh is reduced to 7 €-ct and 4 €-ct for F = 0.5 and F = 1.0, respectively. Note, that these calculations also account for a 2 % discount rate and a 0.5 % annual TEG degradation. Table 3 details the costs of individual components and the steps involved in fabricating the TEGs.

Fig. 14 illustrates the total cost distribution and the weight contribution of each component and step involved in the system building. The plate heat exchanger (PHE) is the most expensive component of this hybrid PHE-TEG system in both cases. Estimated costs of TEG's components, fabrication, and integration into the system are less than 40 % and 50 % of the total cost for fill factors F = 0.5 and F = 1.0, respectively.

4. Conclusion

Numerous low-grade thermal energy resources allow us to apply thermoelectric energy conversion to recycle wasted thermal energy. Printed TEGs present a promising approach for device optimization and fabrication, leveraging additive manufacturing techniques to enable cost-effective production of complex and diverse geometries. In this manuscript, we proposed a hybrid PHE-TEG system for micro-CHP low-grade waste heat recovery from hot water (80 °C). TEG device design and optimization were performed for a corrugated chevron-type plate heat exchanger utilized in district heating applications, employing a Python-implemented model alongside COMSOL simulations. We compared the performance of a simple PHE (without TEGs) and a hybrid PHE-TEG system (with TEGs), highlighting the trade-off between heat transfer and TEG performance. By sacrificing a portion of low-grade heat transfer, the hybrid PHE-TEG system produced high-grade electrical power densities of 355 W/m^2 and 710 W/m^2 for TEG fill factors of F = 0.5 and F = 1.0, respectively, for ideal conditions (i.e., no additional Ohmic losses in the system). Additionally, the total system cost (in €), cost per watt (in €/W), and levelized cost of electricity (LCOE, in €-ct/kWh) were analyzed and reported for two system capacities—one with a 0.5 m^2 area and the other with a 1 m^2 area—at both TEG fill factors. The values for cost per watt (in €/W) and levelized cost of electricity (LCOE, in €-ct/kWh) decreased as the hybrid PHE-TEG system size increased. A system size with 0.5 m^2 area resulted in a cost of electricity of 11.2 €/W and 10 €-ct/kWh for F = 0.5, while for F = 1.0 they were 6.2 €/W and 6 €-ct/kWh. In comparison to 0.5 m^2, 1 m^2 system size showed cost of electricity of 8.1 €/W and 7 €-ct/kWh for F = 0.5, while for F = 1.0 cost values were 4.7 €/W and 4 €-ct/kWh.

Future investigations should delve into incorporating different printed TEGs into other potential energy recovery applications, such as combined heat and power (CHP) systems on large scales, solar thermal systems, geothermal energy systems, seasonal thermal storages, etc.

CRediT authorship contribution statement

Muhammad Irfan Khan: Writing – original draft, Software, Methodology, Investigation, Conceptualization. **Leonard Franke:** Validation, Methodology, Conceptualization. **Andres Georg Rösch:** Writing – review & editing, Methodology, Conceptualization. **Md. Mofasser Mallick:** Writing – review & editing, Conceptualization. **Uli Lemmer:** Writing – review & editing, Supervision, Funding acquisition, Conceptualization.

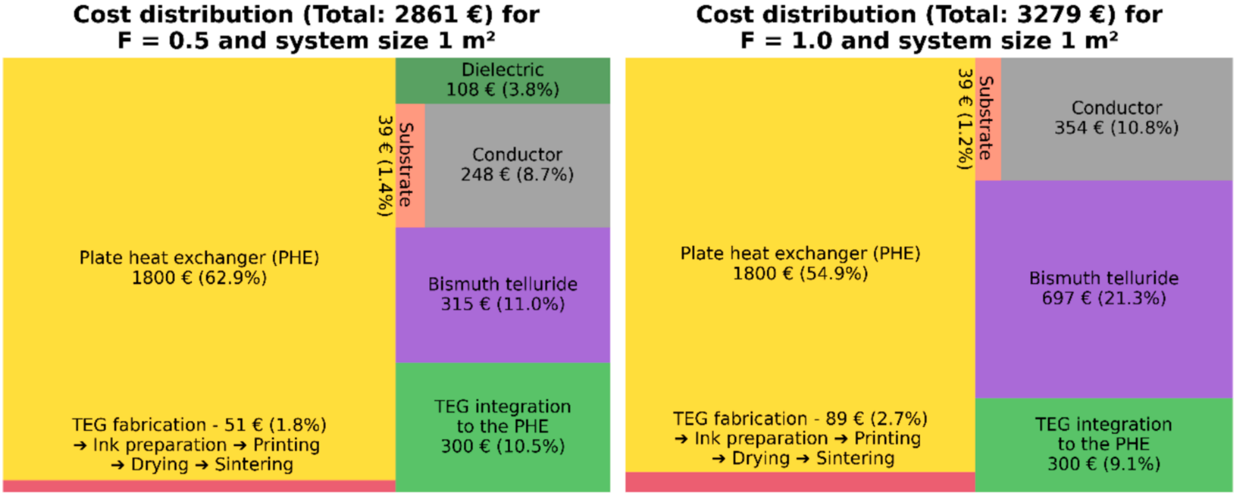

Fig. 14. System total cost distribution for 1 m^2 capacity size (case-I F = 0.5, case-II F = 1.0).

Declaration of competing interest

The authors declare that they have no known competing financial interests or personal relationships that could have appeared to influence the work reported in this paper.

Acknowledgments

The authors acknowledge funding from the Deutsche Forschungsgemeinschaft (DFG, German Research Foundation) under Germany's Excellence Strategy for the Excellence Cluster "3D Matter Made to Order" (EXC – 2082/1 – 390761711), the German Federal Ministry for Economic Affairs and Climate Action through WIPANO project 03THWBW004 for financial support. The German Federal Environmental Foundation (Deutsche Bundesstiftung Umwelt - DBU), through the DBU Ph.D. scholarship program, also supported this work. The authors also wish to acknowledge funding from the Higher Education Commission (HEC) of Pakistan and the German Academic Exchange Service (DAAD). This project has received funding from the European Union's Horizon 2020 research and innovation program under grant agreement no. 814945—SolBio-Rev, and we acknowledge funding by the European Research Council, grant 101097876 - ORTHOGONAL.

Data availability

Data will be made available on request.

References

[1] Johnson I, Choate W, Davidson A. Waste heat recovery. technology and opportunities in U.S. Industry 2008. https://doi.org/10.2172/1218716.
[2] Yazawa K, Shakouri A. Heat flux based optimization of combined heat and power thermoelectric heat exchanger. Energies 2021;14:7791. https://doi.org/10.3390/en14227791.
[3] Starner T. Human-powered wearable computing. IBM Syst J 1996;35:618–29. https://doi.org/10.1147/sj.353.0618.
[4] Solar Energy Research Inst., Golden, CO (USA). ocean thermal energy conversion: an overview. 1989. doi: 10.2172/5390257.
[5] Kaşka Ö. Energy and exergy analysis of an organic Rankine for power generation from waste heat recovery in steel industry. Energ Conver Manage 2014;77:108–17. https://doi.org/10.1016/j.enconman.2013.09.026.
[6] Nowicki C, Gosselin L. An overview of opportunities for waste heat recovery and thermal integration in the primary aluminum industry. JOM 2012;64:990–6. https://doi.org/10.1007/s11837-012-0367-4.
[7] Yazawa K, Shakouri A, Hendricks TJ. Thermoelectric heat recovery from glass melt processes. Energy 2017;118:1035–43. https://doi.org/10.1016/j.energy.2016.10.136.
[8] Ahiska R, Mamur H. Design and implementation of a new portable thermoelectric generator for low geothermal temperatures. IET Renewable Power Gen 2013;7:700–6. https://doi.org/10.1049/iet-rpg.2012.0320.
[9] Attar A, Rady M, Abuhabaya A, Albatati F, Hegab A, Almatrafi E. Performance assessment of using thermoelectric generators for waste heat recovery from vapor compression refrigeration systems. Energies 2021;14:8192. https://doi.org/10.3390/en14238192.
[10] Khan MAI, Khan MI, Kazim AH, Shabir A, Riaz F, Mustafa N, et al. An experimental and comparative performance evaluation of a hybrid photovoltaic-thermoelectric system. Front Energy Res 2021;9:722514. https://doi.org/10.3389/fenrg.2021.722514.
[11] Forman C, Muritala IK, Pardemann R, Meyer B. Estimating the global waste heat potential. Renew Sustain Energy Rev 2016;57:1568–79. https://doi.org/10.1016/j.rser.2015.12.192.
[12] Pourkiaei SM, Ahmadi MH, Sadeghzadeh M, Moosavi S, Pourfayaz F, Chen L, et al. Thermoelectric cooler and thermoelectric generator devices: a review of present and potential applications, modeling and materials. Energy 2019;186:115849. https://doi.org/10.1016/j.energy.2019.07.179.
[13] Champier D. Thermoelectric generators: a review of applications. Energ Conver Manage 2017;140:167–81. https://doi.org/10.1016/j.enconman.2017.02.070.
[14] Fernández-Yáñez P, Romero V, Armas O, Cerretti G. Thermal management of thermoelectric generators for waste energy recovery. Appl Therm Eng 2021;196:117291. https://doi.org/10.1016/j.applthermaleng.2021.117291.
[15] Zhang Y, Wang X, Cleary M, Schoensee L, Kempf N, Richardson J. High-performance nanostructured thermoelectric generators for micro combined heat and power systems. Appl Therm Eng 2016;96:83–7. https://doi.org/10.1016/j.applthermaleng.2015.11.064.
[16] Guoneng L, Youqu Z, Hongkun L, Jiangen H, Jian L, Wenwen G. Micro combined heat and power system based on stove-powered thermoelectric generator. Renew Energy 2020;155:160–71. https://doi.org/10.1016/j.renene.2020.03.130.
[17] Mathiesen BV, Lund H. Comparative analyses of seven technologies to facilitate the integration of fluctuating renewable energy sources. IET Renew Power Gener 2009;3:190–204. https://doi.org/10.1049/iet-rpg:20080049.
[18] Peacock AD, Newborough M. Impact of micro-CHP systems on domestic sector CO$_2$ emissions. Appl Therm Eng 2005;25:2653–76. https://doi.org/10.1016/j.applthermaleng.2005.03.015.
[19] Pellegrini M, Bianchini A. The innovative concept of cold district heating networks: a literature review. Energies 2018;11:236. https://doi.org/10.3390/en11010236.
[20] Østergaard D, Svendsen S. Space heating with ultra-low-temperature district heating – a case study of four single-family houses from the 1980s. Energy Procedia 2017;116:226–35. https://doi.org/10.1016/j.egypro.2017.05.070.
[21] Lund H, Østergaard PA, Chang M, Werner S, Svendsen S, Sorknæs P, et al. The status of 4th generation district heating: research and results. Energy 2018;164:147–59. https://doi.org/10.1016/j.energy.2018.08.206.
[22] Buffa S, Cozzini M, D'Antoni M, Baratieri M, Fedrizzi R. 5th generation district heating and cooling systems: a review of existing cases in Europe. Renew Sustain Energy Rev 2019;104:504–22. https://doi.org/10.1016/j.rser.2018.12.059.
[23] Zheng LJ, Kang HW. A passive evaporative cooling heat sink method for enhancing low-grade waste heat recovery capacity of thermoelectric generators. Energ Conver Manage 2022;251:114931. https://doi.org/10.1016/j.enconman.2021.114931.
[24] Utomo BR, Sulistyanto A, Riyadi TWB, Wijayanta AT. Enhanced performance of combined photovoltaic–thermoelectric generator and heat sink panels with a dual-axis tracking system. Energies 2023;16:2658. https://doi.org/10.3390/en16062658.
[25] Montecucco A, Siviter J, Knox AR. A Combined heat and power system for solid-fuel stoves using thermoelectric generators. Energy Procedia 2015;75:597–602. https://doi.org/10.1016/j.egypro.2015.07.462.
[26] Montecucco A, Siviter J, Knox AR. Combined heat and power system for stoves with thermoelectric generators. Appl Energy 2017;185:1336–42. https://doi.org/10.1016/j.apenergy.2015.10.132.
[27] Lv S, He W, Hu D, Zhu J, Li G, Chen H, et al. Study on a high-performance solar thermoelectric system for combined heat and power. Energ Conver Manage 2017;143:459–69. https://doi.org/10.1016/j.enconman.2017.04.027.
[28] Rösch AG, Franke L, Mallick MM, Lemmer U. Optimizing printed thermoelectric generators with geometry and processibility limitations. Energ Conver Manage 2023;279:116776. https://doi.org/10.1016/j.enconman.2023.116776.
[29] Lund H, Werner S, Wiltshire R, Svendsen S, Thorsen JE, Hvelplund F, et al. 4th Generation district heating (4GDH). Energy 2014;68:1–11. https://doi.org/10.1016/j.energy.2014.02.089.
[30] Martin H. A theoretical approach to predict the performance of chevron-type plate heat exchangers. Chem Eng Process 1996;35:301–10. https://doi.org/10.1016/0255-2701(95)04129-X.
[31] Sahin B, Ust Y, Teke I, Erdem HH. Performance analysis and optimization of heat exchangers: a new thermoeconomic approach. Appl Therm Eng 2010;30:104–9. https://doi.org/10.1016/j.applthermaleng.2009.07.004.
[32] Pike AH. Experimental determination of colburn and friction factors in small plate heat exchangers with high surface enlargement factors. Masters Theses 2012. https://scholarworks.wmich.edu/masters_theses/83/.
[33] Hausen H. Wärmeübertragung im Gegenstrom, Gleichstrom und Kreuzstrom. Springer-Verlag; 2013.
[34] Mallick MM, Franke L, Rösch AG, Geßwein H, Long Z, Eggeler YM, et al. High figure-of-merit telluride-based flexible thermoelectric films through interfacial modification via millisecond photonic-curing for fully printed thermoelectric generators. Adv Sci 2022;9:2202411. https://doi.org/10.1002/advs.202202411.
[35] Ozaeta A, Virtanen P, Bergeret FS, Heikkilä TT. Predicted very large thermoelectric effect in ferromagnet-superconductor junctions in the presence of a spin-splitting magnetic field. Phys Rev Lett 2014;112:057001. https://doi.org/10.1103/PhysRevLett.112.057001.